24th COBEM - 2017

24th ABCM International Congress of Mechanical Engineering
December 3-8, 2017, Curitiba, PR, Brazil

COBEM-2017-0292
NUMERICAL SIMULATIONS OF FLOW AND MIXING FORMATION IN DIRECT INJECTED SPARK IGNITION ENGINES

Mateus Dias Ribeiro, mateusdias@feg.unesp.br
Alex Mendonça Bimbato, alexbimbato@feg.unesp.br
Maurício Araújo Zanardi, mzanardi@feg.unesp.br
José Antônio Perrella Balestieri, perrella@feg.unesp.br
São Paulo State University (UNESP), School of Engineering, Guaratinguetá Campus
Av. Dr. Ariberto Pereira da Cunha, 333, Portal das Colinas, CEP 12.516-410, Guaratinguetá, SP, Brazil

Abstract. *Direct injection spark ignition (DISI) has the potential to reduce specific fuel consumption and therefore, mitigate emissions of state-of-the-art internal combustion engines. Thus, in this work we present numerical simulations of the complex turbulent flow phenomena in DISI engines, as well as the fuel injection and the in-cylinder charge mixing process. For the simulation of turbulence, a large-eddy simulation (LES) methodology is employed and a Lagrangian-Eulerian approach is used to couple the liquid droplet flow with the hot gas inside the combustion chamber. The case of study concerning the engine flow is the Darmstadt optical engine, for which an extensive validation data bank is available. In regard to the fuel-spray injection, the "Spray G" multi-hole gasoline test case provided by the Engine Combustion Network (ECN) is simulated and validated against experimental data. The results obtained so far agree well with the available experimental data, for both cold flow of the Darmstadt engine and "Spray G" simulation cases.*

Keywords: *DISI Engines, Direct Injection, LES, Lagrangian-Eulerian, OpenFOAM*

1. INTRODUCTION

The increasing global concern on greenhouse gases and pollutant emissions has been pushing legislators all over the world to commit to stricter standards for internal combustion engines emission levels. In order to fulfil these commitments, more innovative engine concepts must be developed. Direct injection spark ignition (DISI) is one of these new concepts and it is of crucial importance to the reduction of specific fuel consumption and achievement of the strict emission standards of state-of-the-art internal combustion engines (Goryntsev et al. (2010)).

However, due to design differences, DISI engines may undergo problems such as misfire and poor burning cycles more often than conventional spark ignited engines. This is true because, in the case of DISI engines, the injected fuel has significantly less time to evaporate and form an ignitable gaseous mixture field in the vicinity of the spark-plug than in conventional engines, in which the fuel is already mixed within the gas at spark timing. In order to circumvent these problems, some authors have made important experimental studies to investigate the flame development in DISI engines (Peterson, Reuss, & Sick (2014)). Some of these studies allowed the development of strategies to reduce the existing issues of direct injection in gasoline engines, like the split injection strategy, in which the total amount of fuel is injected in two different instants along intake and compression strokes. Thus, due to the early injection, the fuel mass has enough time to mix adequately inside the engine (Yang & Anderson (1998); Zheng, Tian, & Zhang (2015)).

Concerning numerical simulations of DISI engines, describing the multiphase flow in the combustion chamber relies mainly on either an Eulerian approach, in which liquid and gas phases are described as a continuum, or a Lagrangian approach (often called Lagragian Particle Tracking or LPT approach), in which the fuel droplets are modeled as discrete liquid parcels immersed in a continuum (gas phase). The continuum phases in both strategies are combined with either a Reynolds-averaged Navier-Stokes (RANS) or a large eddy simulation (LES) turbulence framework. Baldwin et al. (2016) developed a novel Eulerian solver to describe the internal and near-nozzle flow of a GDI (gasoline direct injection) injector and many other studies can be found in the literature of engine simulations employing the LPT approach (Lucchini, D'Errico, & Ettorre (2011); Subramaniam (2013)).

Finally, for a long time the RANS/LPT framework has been employed in CFD codes, with moving mesh capabilities and several sub-models, for simulating direct injected engines. However, as pointed out by Richard et al. (2007), only LES is capable of capturing unsteady phenomena occurring in an internal combustion engine such as cyclic variations, that are responsible for the problems of misfire and knocking. Therefore, in this work we have performed a cold flow LES of the Darmstadt engine with a spray-guided cylinder head (Baum et al. (2014)), as well as an LPT/LES of the injection and mixing formation processes of the ECN "Spray G" test case (ECN (2016)).

2. GOVERNING EQUATIONS

The LES filtered governing equations for the balance of mass (1), momentum (2), energy (3), and species (4) read:

$$\frac{\partial \bar{\rho}}{\partial t} + \frac{\partial (\bar{\rho}\tilde{u_j})}{\partial x_j} = S_\rho \tag{1}$$

$$\frac{\partial (\bar{\rho}\tilde{u_i})}{\partial t} + \frac{\partial (\bar{\rho}\tilde{u_i}\tilde{u_j})}{\partial x_j} = \frac{\partial}{\partial x_j}\left[\bar{\rho}\bar{\nu}\left(\frac{\partial \tilde{u_j}}{\partial x_i} + \frac{\partial \tilde{u_i}}{\partial x_j}\right) - \frac{2}{3}\bar{\rho}\bar{\nu}\frac{\partial \tilde{u_k}}{\partial x_k}\delta_{ij} - \bar{\rho}{\tau_{ij}}^{sgs}\right] - \frac{\partial \bar{p}}{\partial x_i} + \bar{\rho}g_i + S_u \tag{2}$$

$$\frac{\partial (\bar{\rho}\tilde{h})}{\partial t} + \frac{\partial (\bar{\rho}\tilde{h}\tilde{u_j})}{\partial x_j} + \frac{\partial (\bar{\rho}\tilde{K})}{\partial t} + \frac{\partial (\bar{\rho}\tilde{K}\tilde{u_j})}{\partial x_j} = \frac{\partial}{\partial x_j}\left(\alpha_{eff}\frac{\partial \tilde{h}}{\partial x_j}\right) + \frac{\partial \bar{p}}{\partial t} + S_h \tag{3}$$

$$\frac{\partial (\bar{\rho}\tilde{Y_i})}{\partial t} + \frac{\partial (\bar{\rho}\tilde{Y_i}\tilde{u_j})}{\partial x_j} = \frac{\partial}{\partial x_j}\left(\mu_{eff}\frac{\partial \tilde{Y_i}}{\partial x_j}\right) + S_{Y_i} \tag{4}$$

In the previous equations, u represents velocity, ρ is the fluid density, ν is the dynamic viscosity, $\mathrm{Y_i}$ is mixture fraction of species i, and g is the acceleration of gravity. The energy equation is solved for the sensible enthalpy h, α_{eff} is the effective thermal diffusivity, and K the kinetic energy. The symbols S_ρ, $\mathrm{S_u}$, $\mathrm{S_h}$ and $\mathrm{S_{Y_i}}$ are source terms added to couple the gas phase with the liquid phase (in case of no fuel injection, all these terms are equal to zero), and μ_{eff} stands for the effective dynamic viscosity. The pressure p is calculated with the pressure-velocity-density coupling algorithm proposed by Demirdžić, Lile, & Perić (1993), which brings robustness to the method, allowing reasonably large steps in time even for high speed flows. The tilde over quantities implies that these equations are operating over the filtered quantities of the fluid of interest and the bar sign means averaging. Furthermore, the sub-grid stresses of the momentum equation, τ_{sgs}, are modeled using the standard Smagorinsky model ($\mathrm{C_s} = 0.168$, Pope (2000)).

The JANAF coefficients are used to calculate the temperature field, and the Sutherland law (Sutherland (1893)) is employed to calculate the viscosity of the mixture. In order to account for the moving parts of the engine such as piston and valves, the equations presented so far must be solved on a moving grid. For this task, a Laplace equation is solved to determine the velocity field of the internal grid elements.

For the fuel injection, the so called parcel approach was used to reduce the necessary computational effort. In this approach, one defines a parcel as a group of droplets with the same properties, and the difficult problem of simulating each particle separately is avoided. Therefore, only bins of particles need to be treated numerically. Another reasonable assumption is to consider that all particles are perfectly spherical, with a diameter d. The size distribution of the injected droplets is modeled by the Rosin-Rammler cumulative density function (CDF), and the velocity magnitude of the parcels is derived from the mass flow rate obtained by experiments and injector geometry properties. Their directions are correlated with expressions that distribute the parcels over a predefined range, in which small particles tend to be injected within an angle (not greater than a maximum value) and the larger particles tend to go straight or to stay within a small angle.

When liquid fuel particles are injected at high velocities in a quiescent gas environment, they are decelerated by the gaseous environment. This exchange of momentum between the liquid and gas phases takes place due to the relative velocity between the two and it is strongly related to the drag coefficient of the fuel droplet, which is calculated using algebraic correlations. Finally, the parcels are tracked in space by updating their positions ($\mathrm{dx_P/dt = u_P}$).

Another consequence of the exchange of momentum between liquid and gas, from the viewpoint of the particle, is the presence of aerodynamic forces that create oscillations on the droplet surface. The increase in amplitude of these oscillations results in droplet breakup. The Weber number $\mathrm{We_P} = \mathrm{u^2_{rel} D\rho_g/\sigma}$ is the relevant parameter for the liquid drop breakup mechanism. This work distinguishes between two kinds of breakup, the bag breakup and the stripping breakup, as described by the model of Reitz & Diwakar (1987).

Ultimately, the liquid droplets and gaseous phase experience heat exchange, for which the appropriate Nusselt number used for calculating the heat transfer coefficient is obtained by the Marshall & Ranz (1952) correlation. When the fuel drop surface reaches the boiling temperature, vaporization takes place. The vaporization process is calculated as described by Zuo, Gomes, & Rutland (2000), taking fuel droplet superheat vaporization into account. The model distinguishes between two kinds of vaporization: vaporization due to flash boiling (calculated with Adachi et al. (1997)'s experimental correlation), and vaporization due to normal heat transfer with the gaseous phase.

3. NUMERICAL SETUP AND VALIDATION CASES

The simulations presented in this work were conducted with the open-source OpenFOAM (Weller et al. (1998)) CFD toolbox, by modifying pre existent solvers (*coldEngineFoam* and *sprayFoam*) to meet the specific purposes of the flow

phenomena studied here. Some setup options are the same for both engine and spray simulations, like the use of the implicit second-order backward scheme for the time integration, and a total diminishing variation (TVD) scheme for dealing with the convective terms of the governing equations. The data used for validation of the engine modeling approach is provided from experiments performed with the Darmstadt optical engine (Baum et al. (2014)) by collaborators from the Technical University of Darmstadt, in Germany. The research gasoline single-cylinder engine is spark ignited and has optical access via a glass liner, as shown in Fig. 1a. The engine has four valves, a flat piston crown, and a pent-roof cylinder head, which allows direct injection from its top. Table 1 shows some characteristics of the Darmstadt engine, and summarizes information on the operation point used for the study in the current work.

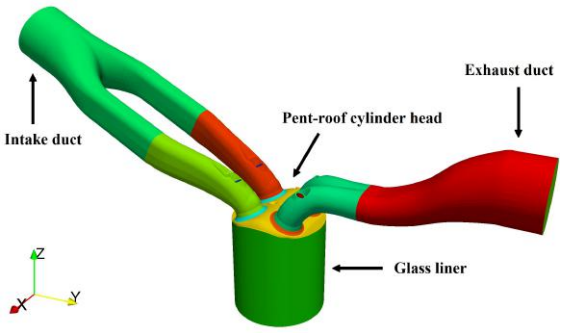

(a) Spray-guided Darmstadt engine (Baum et al. (2014))

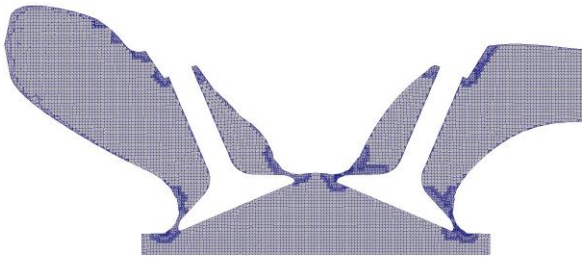

(b) Section of the grid at TDC, showing refinment at the valves

Figure 1: Engine geometry and detail of the grid. This grid resolution produces a total number of 2.75 million cells at top dead center (TDC) and 4.23 million cells at bottom dead center (BDC).

The test-case chosen to validate the proposed fuel-spray model is the "Spray G" from the ECN (Engine Combustion Network), in which a multi-hole gasoline injector is used to inject iso-octane in a quiescent gaseous ambient (Table 2). Fig. 2 illustrates the spray cloud during injection. It is important to note that although each spray jet direction is inclined in reference to the axial direction (z), the penetration length is measured along the z axis, as shown in Fig. 2a.

Table 1: Darmstadt engine, Baum et al. (2014)

Bore /Stroke	86 mm / 86 mm
Displacement	499.6 cm^3
Number of valves	4 (pent-roof cylinder head)
Compression ratio	8.7:1
Engine speed	800 +/- 7 min^{-1}
Intake pressure	0.95 bar
Intake temperature	295 K
Exhaust pressure	1 bar
Exhaust temperature	316.7 K
Intake valve open	35 CAD before TDC
Intake valve close	55 CAD after BDC
Exhaust valve open	75 CAD before BDC
Exhaust valve close	15 CAD after TDC

Table 2: "Spray G", ECN (2016)

Fuel	Iso-octane
Injection pressure	20 MPa
Fuel temperature	90 °C (363 K)
Ambient temperature	300 °C (573 K)
Ambient density	3.5 $\mathrm{kg/m}^3$
Ambient pressure	6 bar (600 kPa)
Ambient composition	89.71% N_2, 6.52% CO_2, 3.77% H_2O
Injected quantity	10 mg
Injection duration	780 μs
Number of nozzle holes	8 (equally spaced)
Hole diameter	165 μm
Fully included angle	80°

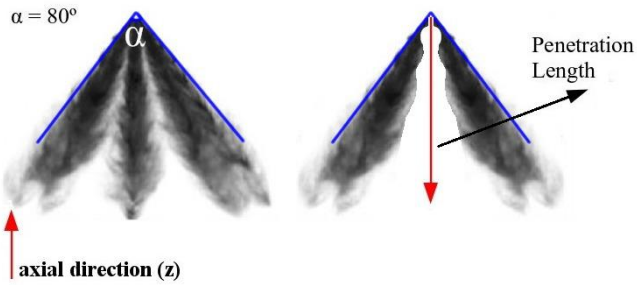

(a) Fuel-spray cloud

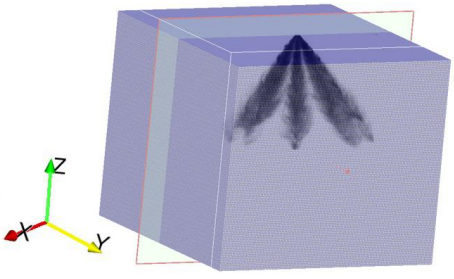

(b) 0.5 mm resolution grid (2.35 million hex. cells)

Figure 2: ECN (2016) "Spray G" test-case and computational mesh.

4. RESULTS AND DISCUSSION

As the studies described in the previous section were done separately, and as they are not directly related to each other (although the Darmstadt engine can be operated with direct injection), the following discussion is divided in two subsections. First, the results concerning the Darmstadt engine simulation are presented, followed by the results of the ECN "Spray G" test case. In the following subsections, the experimental data used for validation of this work was provided to us by different groups (TU Darmstadt and ECN), and the related publications are referenced every time experimental values are presented (please note, however, that some of these results may not be explicitly shown in those publications).

4.1 Darmstadt engine simulation

For simulating the Darmstadt engine, a mapping strategy was employed to maintain high mesh quality as piston and valves move. In this strategy, the whole engine cycle is split into equally spaced intervals of 5 crank angle degrees (CAD). After performing one interval, the simulation is stopped and the results are mapped onto a new grid without deformed cells. Simulation begins at TDC, when the intake valves are starting to open, exhaust valves are finishing their closure, and piston is moving down at an engine speed of 800 rpm. Time-varying absolute pressure boundary conditions are applied on the inlet and outlet surfaces, using experimental data. The intake temperature is fixed at 295 K and the wall temperatures are fixed at 333 K. The simulation comprehended two entire cold flow cycles, taking approximately 4 months of computational time, with adjustable time step set to a maximum Courant-Friedrich-Lewy (CFL) number of 0.5.

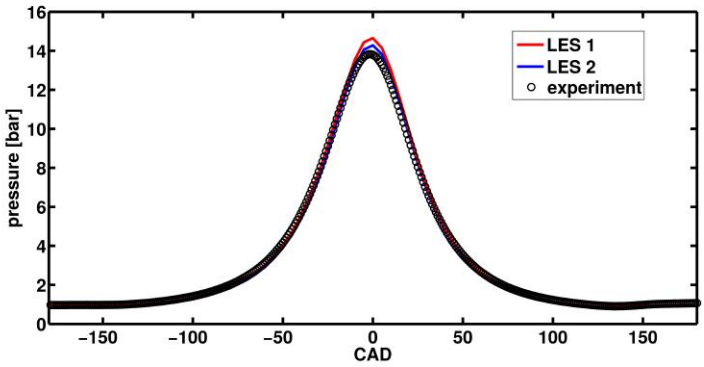

Figure 3: Pressure trace inside the combustion chamber, LES vs. experiment (performed by Peterson et al. (2017)).

Fig. 3 shows the pressure trace along compression and expansion strokes of both LES cycles, and measured values obtained by collaborators at TU Darmstadt (Peterson et al. (2017)) on the same plot. Negative CAD values mean time instants before TDC (bTDC) and positive ones mean instants after TDC (aTDC). The agreement between simulation and experiment is very good (error under 1%) until 25 CAD bTDC and after 40 CAD aTDC. Within the aforementioned period, the pressure in the simulation starts to deviate slightly from the pressure in the experiment. The peak deviation occurs at TDC and has a value of 6.2% for the first cycle and 3.6% for the second. This small deviation is explained because of the under-prediction of heat loss by not representing the the top-land crevice (the volume surrounded by the liner, piston and the highest seal ring). If considered, that error vanishes, as shown by Janas (2016) for the same engine.

In Fig. 4 and Fig. 5, plots of the flow field of the first cycle on a plane over two of the valves and on the central plane for 270 bTDC and 180 bTDC are presented. For each figure, the z (axial) and y (radial) components of the velocity field are shown. By analysing these plots, it is possible to see that a tumble motion starts to form at -270 CAD by the action of the high velocity flow through the valves and it gets very clear at -180 CAD, especially on the central plane (Fig. 5c shows ascending axial velocities on the left portion of the plane with descending axial velocities on the right, while Fig. 5d shows positive radial velocities on the top and negative radial velocities on the bottom, which indicates a big vortex motion in the clockwise direction). The presence of a tumble vortex and its center position can also be determined in a more quantitative manner, by applying the algorithm proposed by Graftieaux, Michard, & Grosjean (2001), as shown in Eq.5:

$$\Gamma(p) = \frac{1}{N} \sum_{S} \frac{(PM \wedge U_M) \cdot z}{||PM|| \cdot ||U_M||} \tag{5}$$

With this algorithm, the center of the vortex in a bi-dimensional velocity field (y and z velocity components of Fig. 4 and Fig. 5) is determined by calculating the parameter Γ, for which N is the number of points inside the sampled area S, P is the vortex center, M is a point lying in S, z is the unit vector normal to the plane, and U_M is the velocity vector. The vortex center lies in the point where Γ is maximum (normally close to 1). The algorithm was applied on the central plane of the simulations to determine the evolution of the vortex center from -180 CAD until -10 CAD, as shown in Fig. 6.

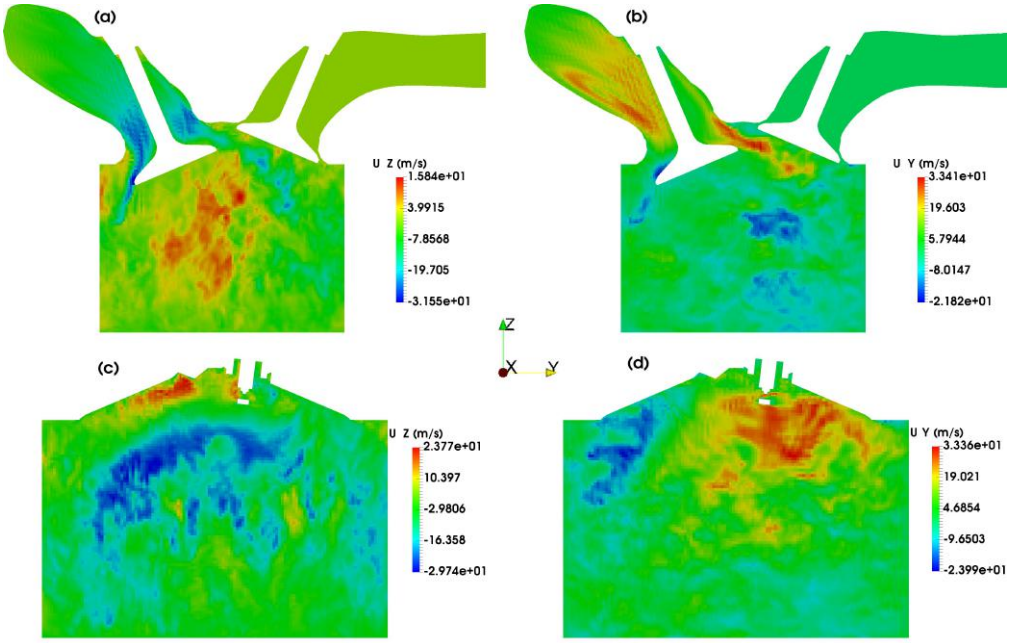

Figure 4: Flow field at -270 CAD, first cycle. (a) axial velocity field on plane over the valves, (b) radial velocity field on plane over the valves and (c) axial velocity on central plane, (d) radial velocity on central plane.

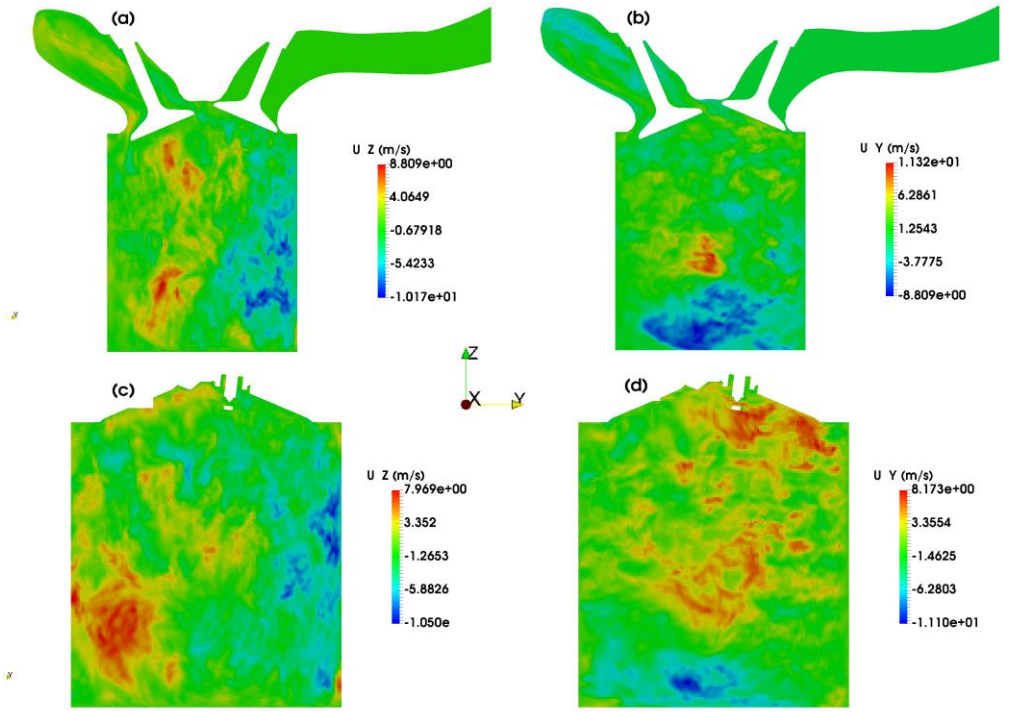

Figure 5: Flow field at -180 CAD, first cycle. (a) axial velocity field on plane over the valves, (b) radial velocity field on plane over the valves and (c) axial velocity on central plane, (d) radial velocity on central plane.

For the closure of the results regarding the Darmstadt engine, the authors were interested in the amount of residual turbulence present in the combustion chamber at the final instants of the compression stroke, since this information may be useful when fired simulations are performed in the future. For this, two sampling lines are defined along the radial axis (y) at the central plane (x = 0), for two different axial positions (z). The first sampling line lies exactly at the beginning of the cylinder liner (z = 0), and the second one lies 5 mm above it (z = 5mm). For each of these sampling lines, radial (y) and axial (z) velocity components (averaged over two cycles) are plotted for CADs ranging from 45 bTDC until TDC, in Fig. 7 and Fig. 8, respectively. The results are validated with experimental values averaged over 80 cycles performed by colleagues from TU Darmstadt (the experiment is presented in Freudenhammer et al. (2015).

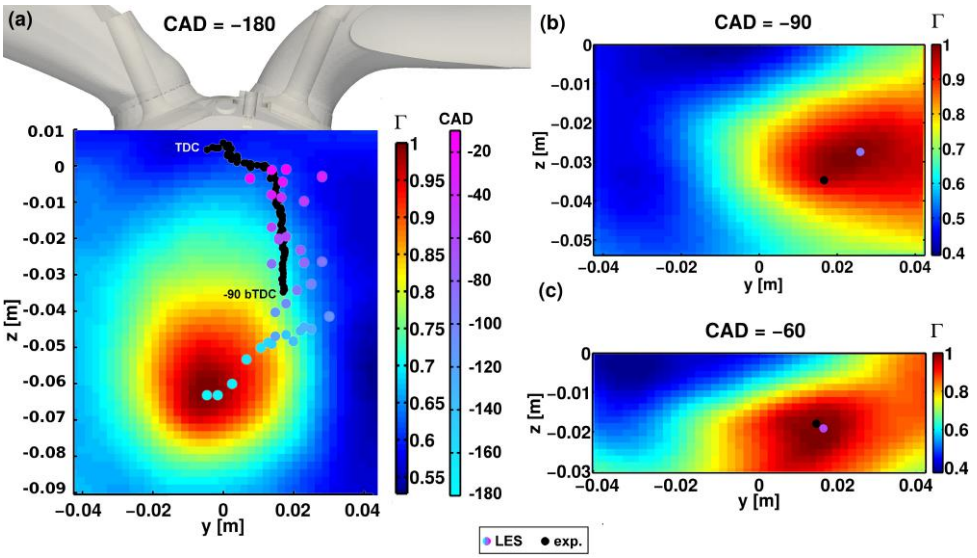

Figure 6: Tumble center vs. time using the vortex center finder algorithm by Graftieaux, Michard, & Grosjean (2001). (a) vortex center plot at -180 CAD, with center positions plotted along time from -180 to -10 CAD (LES) and -90 to TDC (measurements by Freudenhammer et al. (2015)), (b) vortex center at -90 CAD, and (c) vortex center at -60 CAD.

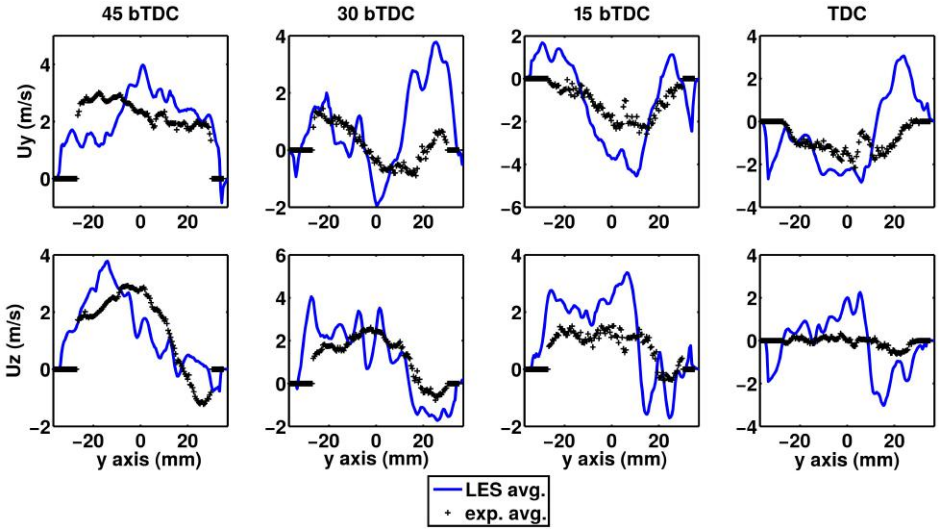

Figure 7: Velocity profile line 1: z = 0 mm, x = 0 mm. Sim. (blue), measurements by Freudenhammer et al. (2015) (black)

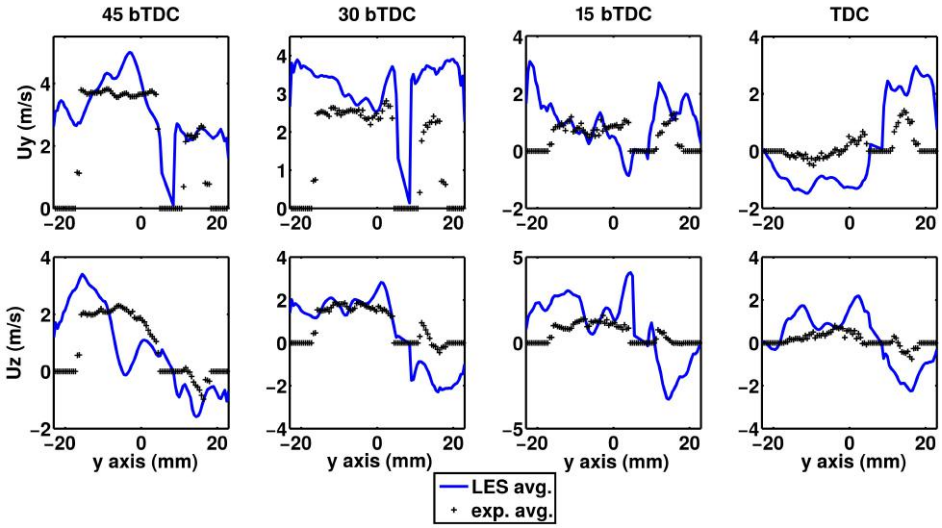

Figure 8: Velocity profile line 2: z = 5 mm, x = 0 mm. Sim. (blue), measurements by Freudenhammer et al. (2015) (black)

4.2 ECN "Spray G" simulation

The spray simulation comprehends a time of 2 ms, from which almost 0.8 ms is the injection duration time. In this way, one can not only see the several phenomena taking place during the fuel injection, but also the mix formation after the injector needle is closed. To guarantee small steps in time, in order to avoid instabilities, an adjustable time step was set to a CFL number of 0.1. We begin showing some plots of the spray simulation in two different instants, in Fig. 9 and Fig. 10 (the first instant, 0.6 ms after start of injection (ASOI), and the second, 1.0 ms ASOI).

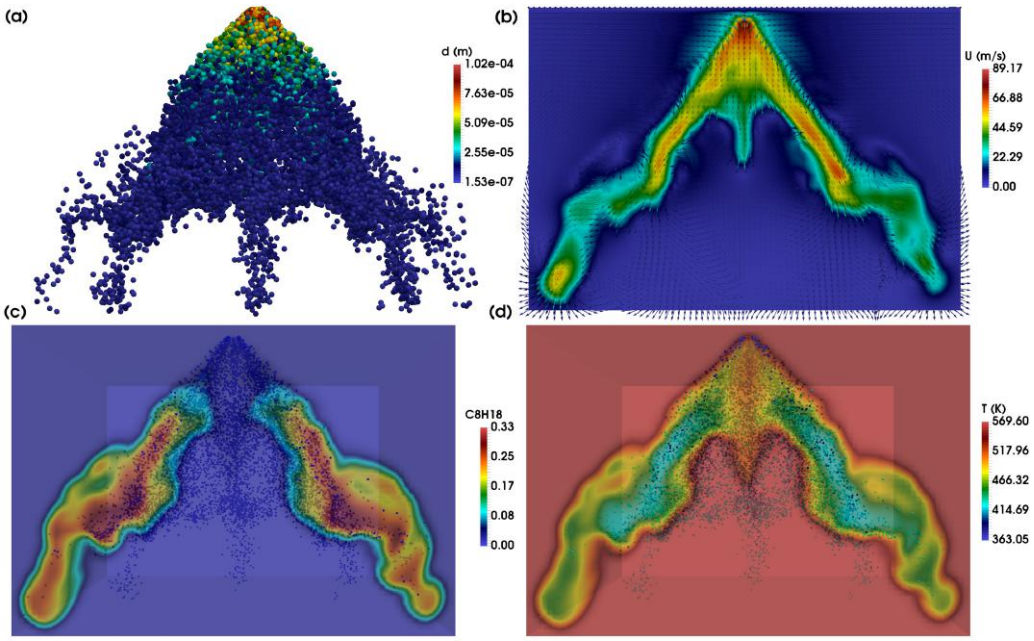

Figure 9: Simulation time = 0.6 ms ASOI. (a) droplet diameter distribution, (b) velocity magnitude profile on central plane, (c) iso-octane mixture fraction profile on central plane, and (d) temperature profile on central plane (d).

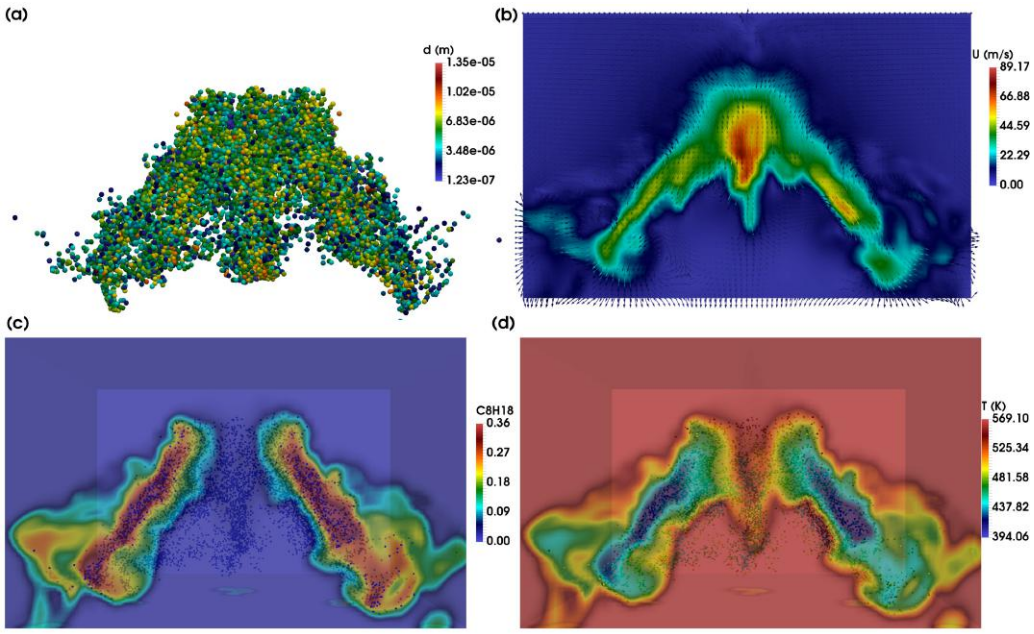

Figure 10: Simulation time = 1.0 ms ASOI. (a) droplet diameter distribution, (b) velocity magnitude profile on central plane, (c) iso-octane mixture fraction profile on central plane, and (d) temperature profile on central plane (d).

In the previous figures, four different quantities are shown on the central plane of the domain. First, the droplet size distribution, ranging from the injected droplet diameter of around 100 μm until something as small as 0.1 μm, after end of injection and with the droplets being subject to breakup and vaporization for enough time. Second, the velocity magnitude of the gaseous phase, showing the high injection velocities induced by the high internal nozzle pressure. Then,

the iso-octane mixture fraction and, finally, the temperature field in the gaseous phase. Furthermore, Fig. 11 shows the vapor and liquid penetration along time, comparing the results obtained in the simulation with experimental data obtained by contributors of the ECN. The agreement of the vapor penetration length is very good until end of injection (0.78 ms), but it starts to deviate slightly from the experimental result after that. The liquid penetration length is also quite good prior to the end of injection, although it diverges highly from the measured data after that, taking more than 0.2 ms more to have all liquid phase vanished. Fig. 12a shows in the same plot, the number of parcels and the evaporated mass along time. As expected, the number of parcels increases continually until end of injection, from which point it starts to decrease until all the liquid is evaporated, adding more mass to the gas phase. In Fig. 12b, the maximum and the Sauter mean diameter (D32) of the droplets are plotted, showing an average volume per surface based diameter around 60 μm at the start of injection and somewhat lower than 20 μm just after needle closure.

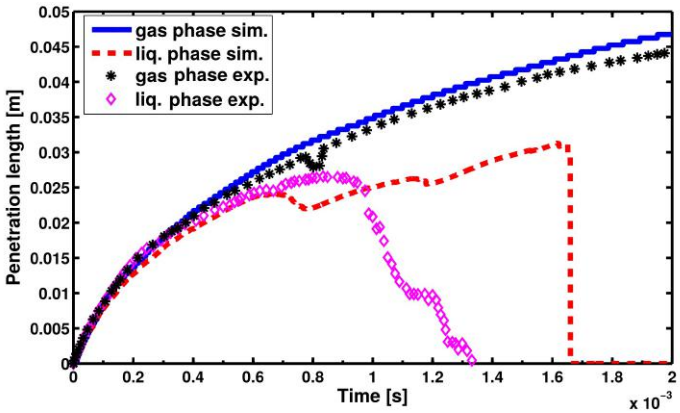

Figure 11: Vapor and liquid penetration length along time. LES vs. experiment (ECN (2016)).

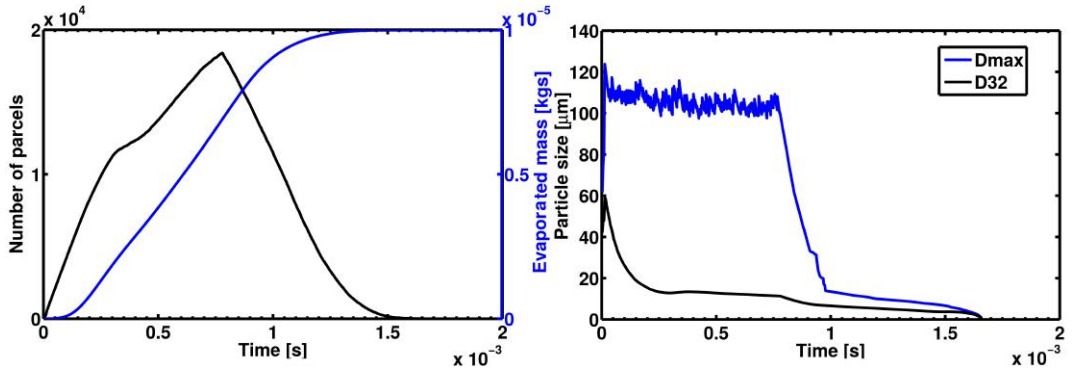

Figure 12: (a) number of parcels and evaporated mass, (b) maximum diameter and Sauter-mean diameter.

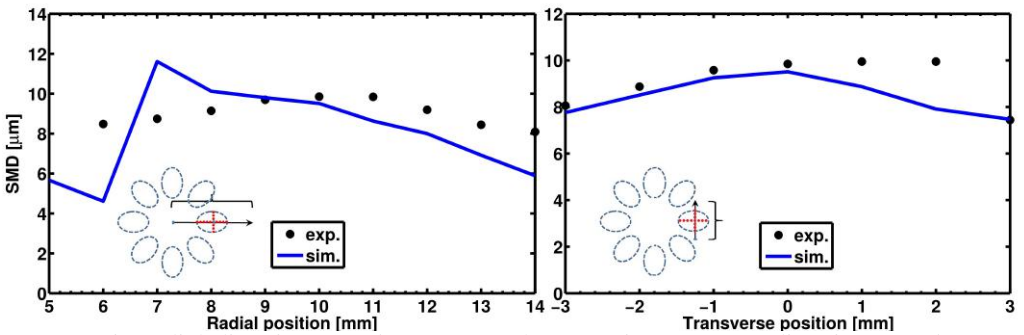

Figure 13: (a) SMD in radial direction at 0.5 ms ASOI, (b) SMD in transverse direction at 0.5 ms ASOI. LES vs. experiment (ECN (2016)).

In Figures 13 and 14, the Sauter mean diameter in positions along a sampling line defined by the ECN guidelines are shown in comparison to the experimental values for times 0.5 ms and 0.6 ms after start of injection. Using the same sampling lines and for the same times, the droplet axial velocities in the simulation are compared to the measured ones in

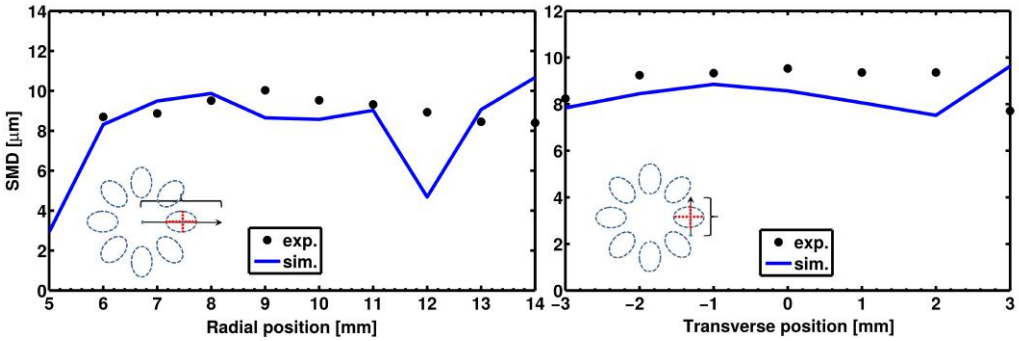

Figure 14: (a) SMD in radial direction at 0.6 ms ASOI, (b) SMD in transverse direction at 0.6 ms ASOI. LES vs. experiment (ECN (2016)).

Figures 15 and 16. The first sampling line (plots on the left) is a line starting 15 mm below the nozzle position and that follows one of the 8 jets produced by the multi-hole injector along the radial axis. The second sampling line (plots on the right) also starts 15 mm below the nozzle location but follows a line perpendicular to the first line, passing through the center of the jet plume. Overall, the model shows reasonably good agreement with the experiment.

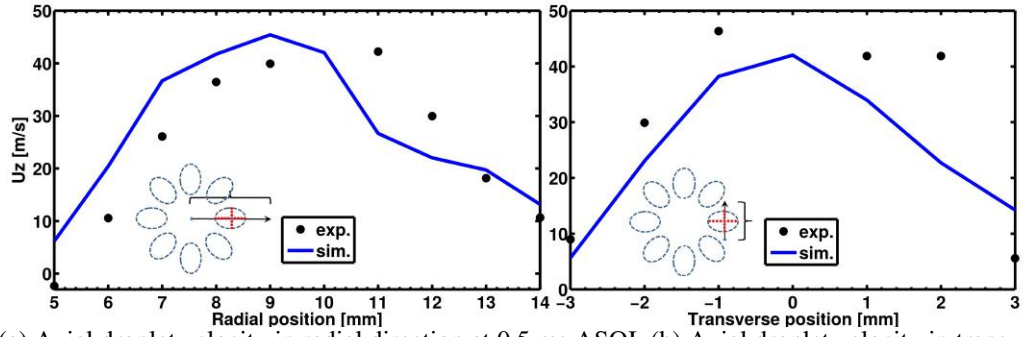

Figure 15: (a) Axial droplet velocity in radial direction at 0.5 ms ASOI, (b) Axial droplet velocity in transverse direction at 0.5 ms ASOI. LES vs. experiment (ECN (2016)).

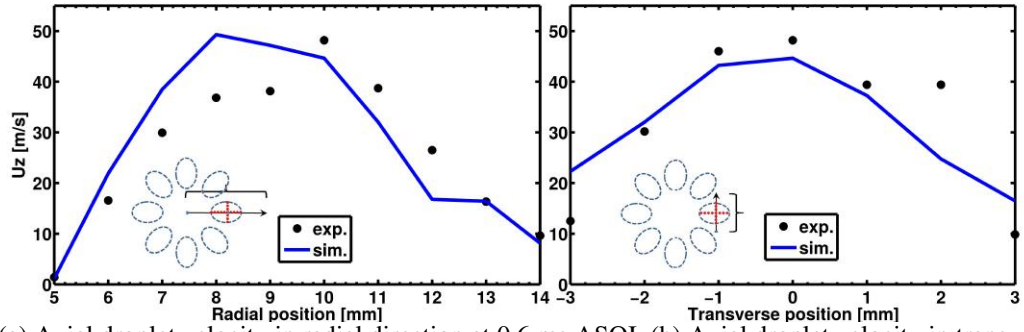

Figure 16: (a) Axial droplet velocity in radial direction at 0.6 ms ASOI, (b) Axial droplet velocity in transverse direction at 0.6 ms ASOI. LES vs. experiment (ECN (2016)).

5. CONCLUSIONS

This paper presented some preliminary simulations of two entire cold flow cycles of the Darmstadt optical engine, as well as simulations of the ECN "Spray G" multi-hole gasoline injection test case. These studies are of great importance due to the increasing trend of using direct injection in gasoline engines in order to reduce fuel consumption and greenhouse gas emissions. When validated with experimental data provided by different groups, both simulations have shown good results. For future works, the authors aim to perform spray simulations in a moving mesh framework, so that later motored and fired simulations of the Darmstadt engine with direct injection can be carried out.

ACKNOWLEDGEMENTS

The authors acknowledge the financial support by FAPESP (Process 2015/10299-9), the TU Darmstadt for providing the engine CAD and validation data, and the Engine Combustion Network for providing the spray validation data.

6. REFERENCES

Adachi, M, McDonell, V. G., Tanaka, D, Senda, J, & Fujimoto, H, 1997. Characterization of Fuel Vapor Concentration Inside a Flash Boiling Spray. *SAE Technical Paper*, no. 970871.

Baldwin, E., GROVER Jr., R., Parrish, S., Duke, D., Matusik, K., Powell, C., Kastengren, A., & Schmidt, D., 2016. String flash-boiling in gasoline direct injection simulations with transient needle motion. *International Journal of Multiphase Flow*, vol. 87, pp. 90–101.

Baum, E., Peterson, B., Böhm, B., & Dreizler, A., 2014. On The Validation of LES Applied to Internal Combustion Engine Flows: Part 1: Comprehensive Experimental Database. *Flow, Turbulence and Combustion*, vol. 92, no. 1, pp. 269–297.

Demirdžić, I., Lile, Ž., & Perić, M., 1993. A collocated finite volume method for predicting flows at all speeds. *International journal for numerical methods in fluids*, vol. 16, pp. 1029–2050.

ECN, 2016. Spray G operation conditions. <http://www.sandia.gov/ecn/G/targetCondition/sprayG.php>. Accessed on: October 27, 2016.

Freudenhammer, D., Peterson, B., Ding, C.-P., Boehm, B., & Grundmann, S., 2015. The Influence of Cylinder Head Geometry Variations on the Volumetric Intake Flow Captured by Magnetic Resonance Velocimetry. *SAE Int. J. Engines*, vol. 8, pp. 1826–1836. URL: https://doi.org/10.4271/2015-01-1697.

Goryntsev, D, Sadiki, A, Klein, M, & Janicka, J, 2010. Analysis of cyclic variations of liquid fuel-air mixing processes in a realistic DISI IC-engine using Large Eddy Simulation. *International Journal of Heat and Fluid Flow*, vol. 31, pp. 845–849.

Graftieaux, L., Michard, M., & Grosjean, N., 2001. Combining PIV, POD and vortex identification algorithms for the study of unsteady turbulent swirling flows. *Measurement Science And Technology*, vol. 12, pp. 1422–1429.

Janas, P., 2016. Numerical Investigation of the Influence of Different Valve Seat Geometries on the In-Cylinder Flow and Combustion in Spark Ignition Engines. <http://www.rs-les4ice.com/Projet/upload/docs/application/pdf/2016-12/2_les4ice_janas.pdf>. Accessed: 15th Aug 2017.

Lucchini, T, D'Errico, G, & Ettorre, D, 2011. Numerical investigation of the spray-mesh-turbulence interactions for high-pressure, evaporating sprays at engine conditions. *Int. Journal of Heat and Fluid Flow*, vol. 32, pp. 285–297.

Marshall, W. R. & Ranz, W. E., 1952. Internal Combustion Engine Modeling. Hemisphere Publishing.

Peterson, B., Baum, E., Ding, C.-P., Michaelis, D., Dreizler, A., & Böhm, B., 2017. Assessment and application of tomographic PIV for the spray-induced flow in an IC engine. *Proceedings of the Combustion Institute*, vol. 36, no. 3, pp. 3467 –3475. ISSN: 1540-7489.

Peterson, B., Reuss, D. L., & Sick, V., 2014. On the ignition and flame development in a spray-guided direct-injection spark-ignition engine. *Combustion and Flame*, vol. 161, pp. 240–255.

Pope, S. B., 2000. Turbulent Flows. Cambridge University Press.

Reitz, R. D. & Diwakar, R, 1987. Structure of High-Pressure Fuel Sprays. *SAE Technical Paper*, no. 870598.

Richard, S., Colin, O., Vermorel, O., Benkenida, A., Angelberger, C., & Veynante, D., 2007. Towards large eddy simulation of combustion in spark ignition engines. *Proceedings of the Combustion Institute*, vol. 31, pp. 3059–3066.

Subramaniam, S., 2013. Lagrangian-Eulerian methods for multiphase flows. *Progress in Energy and Combustion Science*, vol. 39, pp. 215–245.

Sutherland, W., 1893. The viscosity of gases and molecular force. *Philosophical Magazine Series 5*, vol. 36:223, pp. 507–531. DOI: 10.1080/14786449308620508.

Weller, H. G., Tabor, G., Jasak, H., & Fureby, C., 1998. A tensorial approach to computational continuum mechanics using object-oriented techniques. *Computer in Physics*, vol. 12, pp. 620–631.

Yang, J. L. & Anderson, R. W., 1998. Fuel Injection Strategies to Increase Full-Load Torque Output of a Direct-injection SI Engine. *SAE Technical Paper*, no. 980495.

Zheng, Z., Tian, X., & Zhang, X., 2015. Effects of split injection proportion and the second injection time on the mixture formation in a GDI engine under catalyst heating mode using stratified charge strategy. *Applied Thermal Engineering*, vol. 84, pp. 237–245.

Zuo, B, Gomes, A. M., & Rutland, C. J., 2000. Modelling superheated fuel sprays and vaporization. *Int J Engine Research*, vol. 1, pp. 321–336.

7. RESPONSIBILITY NOTICE

The authors are the only responsible for the printed material included in this paper.